

Probing and manipulating valley coherence of dark excitons in monolayer WSe₂

M. R. Molas,^{1,2,*} A. O. Slobodeniuk,¹ T. Kazimierczuk,² K. Nogajewski,^{1,2} M. Bartos,¹ P. Kapuściński,^{1,3} K. Oreszczuk,² K. Watanabe,⁴ T. Taniguchi,⁴ C. Faugeras,¹ P. Kossacki,² D. M. Basko,⁵ and M. Potemski^{1,2,†}

¹*Laboratoire National des Champs Magnétiques Intenses, CNRS-UGA-UPS-INSA-EMFL, 25 avenue des Martyrs, 38042 Grenoble, France*

²*Institute of Experimental Physics, Faculty of Physics, University of Warsaw, ul. Pasteura 5, 02-093 Warszawa, Poland*

³*Department of Experimental Physics, Faculty of Fundamental Problems of Technology, Wrocław University of Science and Technology, 27 Wybrzeże Wyspiańskiego, 50-370 Wrocław, Poland*

⁴*National Institute for Materials Science, 1-1 Namiki, Tsukuba 305-0044, Japan*

⁵*Laboratoire de Physique et Modélisation des Milieux Condensés, Université Grenoble Alpes and CNRS, 25 avenue des Martyrs, 38042 Grenoble, France*

Monolayers of semiconducting transition metal dichalcogenides are two-dimensional direct-gap systems which host tightly-bound excitons with an internal degree of freedom corresponding to the valley of the constituting carriers. Strong spin-orbit interaction and the resulting ordering of the spin-split subbands in the valence and conduction bands makes the lowest-lying excitons in WX₂ (X being S or Se) spin-forbidden and optically dark. With polarization-resolved photoluminescence experiments performed on a WSe₂ monolayer encapsulated in a hexagonal boron nitride, we show how the intrinsic exchange interaction in combination with the applied in-plane and/or out-of-plane magnetic fields enables one to probe and manipulate the valley degree of freedom of the dark excitons.

Monolayers of transition metal dichalcogenides (TMDs), such as MX₂ with M=Mo or W, and X=S, Se or Te, are two-dimensional direct-gap semiconductors¹ which attract a lot of interest due to their unique physical properties and potential applications in optoelectronics, photonics and the development of valleytronics^{2-5,7,18}. The direct bandgap in semiconducting TMDs (S-TMDs) is located at the two inequivalent \mathbf{K}_{\pm} points (valleys) of the first Brillouin zone, related by time reversal symmetry. In monolayers, the tightly bound and optically bright excitons⁸⁻¹¹ from \mathbf{K}_{\pm} valley can efficiently couple to light with right/left circular polarization^{12,13}, respectively.

A unique feature of S-TMD monolayers is the so-called spin-valley locking¹³: strong spin-orbit interaction lifts the degeneracy between the two spin projections $s = \uparrow, \downarrow$ in each valley, leaving only the Kramers degeneracy between the opposite valleys, $\mathbf{K}_{+}, s \leftrightarrow \mathbf{K}_{-}, -s$. While the valence band spin-orbit splitting Δ_v is very large (several hundred meV¹³), its conduction band counterpart Δ_c is by an order of magnitude smaller¹⁴⁻¹⁸, thus allowing some degree of manipulation by an in-plane magnetic field. In tungsten-based S-TMDs, Δ_c has the same sign as Δ_v , leading to the spin subband ordering shown in Fig. 1(a). In each valley, the optically bright exciton has a higher energy than the dark exciton which is composed of the conduction and valence electronic states with opposite spin projections. This, among other things, results in a strong temperature dependence of the photoluminescence (PL) efficiency, as the bright states become more populated at higher temperatures^{8,19,21}.

Dark excitons can couple to light only via a residual spin-flip dipole matrix element d_{\perp} , whose direction is perpendicular to the monolayer plane²²⁻²⁴. In consequence, the emission of dark excitons is directed predominantly

along the monolayer plane, in contrast to the out-of-plane emission of bright excitons characterized by strong in-plane optical dipoles, d_{\parallel} , see Fig. 1(b). Notably, the valley degeneracy of dark excitons is lifted by the exchange interaction which mixes the valleys and produces two eigenstates with different energies. The higher energy component takes up the whole oscillator strength due to d_{\perp} (so we call it “grey”), while the low-energy component is completely decoupled from light and truly “dark”^{23,25}.

The possibility to control the valley degree of freedom for bright excitons by optical polarization²⁶⁻²⁸ and external magnetic field^{12,30,31} is impaired by the quick valley relaxation due to the exchange interaction^{22,32}, because the latter (i) depends on the exciton center-of-mass momentum, and (ii) is considerably strong, being governed by the same (large) in-plane dipole moment d_{\parallel} as the optical transitions. For dark excitons, the exchange interaction is (i) a short-range local field effect, so it weakly depends on momentum, (ii) strong enough to produce a sizeable dark- grey splitting $\delta \approx 0.6\text{meV} \approx 7\text{K}$ in WSe₂¹⁰ which makes the dark component dominant at low temperatures, and (iii) at the same time weak enough to enable a control of the splitting and of the valley content by a perpendicular magnetic field B_{\perp} of a few Tesla¹⁰. Importantly, by applying an in-plane magnetic field B_{\parallel} , one can transfer the in-plane oscillator strength from the higher-energy bright states to the dark-grey doublet^{17,18}, thus boosting the out-of-plane emission of light from both components of this doublet.

In this work we present an experimental implementation of the described “dark exciton valley toolkit” in a WSe₂ monolayer. Namely, we investigate the influence of the in-plane and/or out-of-plane magnetic fields on dark excitons emission. In particular, we experimentally

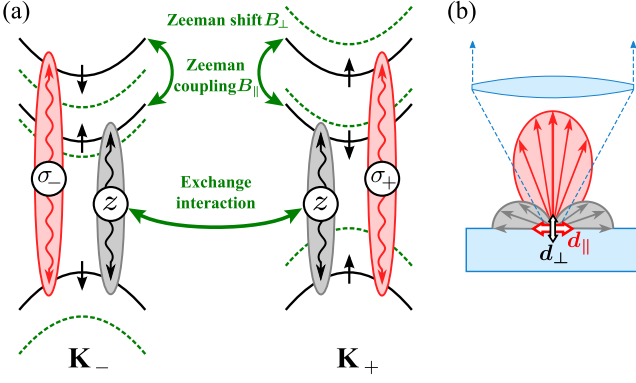


FIG. 1. (a) Spin and valley structure of WSe₂. Black solid curves show the spin-split bands in the \mathbf{K}_{\pm} valleys at zero magnetic field, the spin projections are indicated by black arrows. Grey and red ellipses represent spin-forbidden and spin-allowed excitonic transitions in each valley, respectively. Dashed green curves show Zeeman-shifted bands in a perpendicular magnetic field. Thick green arrows represent the exchange interaction which mixes the two valleys, and the Zeeman coupling in an in-plane magnetic field which mixes different spin subbands in the same valley. (b) A schematic representation of radiation patterns of dark and bright excitons in S-TMD monolayer at zero magnetic field. The grey (red) arrows indicate the propagation direction of the light, emitted by dark (bright) excitons. The blue dashed lines define the region of light collected by the lens. The black and red double-headed arrows depict the relative magnitudes and directions of out-of-plane (d_{\perp}) and in-plane (d_{\parallel}) dipoles.

demonstrate the coherent valley-superposition nature of the dark and grey excitons by transferring the oscillator strength from the bright excitons with an in-plane magnetic field and detecting a linearly polarized luminescence. We use a WSe₂ sample encapsulated in hexagonal boron nitride (hBN), which is known to significantly enhance the sample quality^{34–38}. In our experiment, the encapsulation leads to a very strong brightening effect, much more pronounced than observed earlier^{17,18}, and enables us to spectrally resolve the fine structure of the brightened dark excitons. We observed that the combination of the in-plane and out-of-plane magnetic fields leads to circularly-polarized emissions due to the dark and grey excitons.

The valley structure of intravalley excitons in a magnetic field of arbitrary orientation can be described using the model of Refs 10,17,23. Let us work in the basis of the four intravalley A-exciton states with zero center-of-mass momentum at zero magnetic field. These states $|\mathbf{K}_{\pm}, s_c\rangle$ can be identified by the valley \mathbf{K}_{\pm} and the conduction band spin projection $s_c = \uparrow, \downarrow$. The valence band spin projection is fixed for the A exciton: $s_v = \uparrow$ in \mathbf{K}_+ valley and \downarrow in \mathbf{K}_- . The states $|\mathbf{K}_+, \uparrow\rangle$, $|\mathbf{K}_-, \downarrow\rangle$ are bright and are denoted by $|\mathbf{K}_{\pm}, b\rangle$, respectively. Their transition dipole matrix elements lie in the plane and correspond to the two circular polarizations, $\langle 0|\hat{\mathbf{d}}|\mathbf{K}_{\pm}, b\rangle = -id_{\parallel}(\pm\mathbf{e}_x + i\mathbf{e}_y)$. The states

$|\mathbf{K}_+, \downarrow\rangle$, $|\mathbf{K}_-, \uparrow\rangle$ are denoted as $|\mathbf{K}_{\pm}, d\rangle$ and have transition dipoles $\langle 0|\hat{\mathbf{d}}|\mathbf{K}_{\pm}, d\rangle = id_{\perp}\mathbf{e}_z$, perpendicular to the plane^{10,22–24,39}, $d_{\perp}/d_{\parallel} \sim 0.01 - 0.1$ ²³.

In the basis $|\mathbf{K}_+, b\rangle$, $|\mathbf{K}_-, b\rangle$, $|\mathbf{K}_+, d\rangle$, $|\mathbf{K}_-, d\rangle$, the Hamiltonian matrix has the form

$$H = \begin{bmatrix} \Delta + g_b\mathcal{B}_z & 0 & g_{\parallel}\mathcal{B}_- & 0 \\ 0 & \Delta - g_b\mathcal{B}_z & 0 & g_{\parallel}\mathcal{B}_+ \\ g_{\parallel}\mathcal{B}_+ & 0 & \delta/2 + g_d\mathcal{B}_z & \delta/2 \\ 0 & g_{\parallel}\mathcal{B}_- & \delta/2 & \delta/2 - g_d\mathcal{B}_z \end{bmatrix}. \quad (1)$$

Counting energies from the dark exciton state, we denote by $\Delta \approx 40$ meV^{10,17,18,24} and $\delta \approx 0.6$ meV¹⁰, respectively, the dark-bright and dark-grey splitting at zero field. The parameter δ characterizes the short-range exchange interaction which lifts the valley degeneracy of the dark excitons at $B_{\perp} = 0$ and forms two new (grey and dark) eigenstates: $|\mathbf{G}\rangle, |\mathbf{D}\rangle = (|\mathbf{K}_+, d\rangle \pm |\mathbf{K}_-, d\rangle)/\sqrt{2}$.

Other terms in equation (1) describe the effect of the magnetic field, of the in-plane component, B_{\parallel} , and of the perpendicular one, B_{\perp} ; we use the shorthand notation $\mathcal{B}_z \equiv \mu_B B_{\perp}/2$, $\mathcal{B}_{\pm} \equiv \mu_B(B_x \pm iB_y)/2$, where $\mu_B = 57.88\mu\text{eV/T}$ is the Bohr magneton. The perpendicular field B_{\perp} lifts the single-electron Kramers degeneracy between opposite spins in opposite valleys. This results in a valley-dependent shift of the excitonic levels with different Landé factors in the bright and dark-grey sectors. The in-plane magnetic field $\mathbf{B}_{\parallel} = (B_x, B_y)$ produces the Zeeman coupling ($g_{\parallel}\mu_B B_{\parallel}$) of the electronic states with opposite spins in the same valley, and thus mixes the dark-grey and bright excitonic sectors, remaining diagonal in the valley index.

The magnetic field terms in Hamiltonian (1) provide the experimental tools which enable one to control and probe the dark exciton states. At $B_{\parallel} = 0$, one can tune continuously the valley content of the dark and grey excitons by changing B_{\perp} . Then, turning on the B_{\parallel} field, one admixes the bright states to the dark-grey sector, thereby transferring the in-plane oscillator strength; since Δ is the largest energy scale in Hamiltonian (1), this admixture can be treated perturbatively. Then, it turns out that the valley content of the eigenstates in the dark-grey sector can be probed by measuring linear polarization of the light emitted now in the direction perpendicular to the monolayer plane. Consider an eigenstate $|\psi_d\rangle$ at $B_{\parallel} = 0$ in the form of a general linear combination, $|\psi_d\rangle = \chi_+ e^{i\phi_d} |\mathbf{K}_+, d\rangle + \chi_- e^{-i\phi_d} |\mathbf{K}_-, d\rangle$ with real χ_{\pm} , $\chi_+^2 + \chi_-^2 = 1$ and some phase ϕ_d . Let us apply B_{\parallel} and detect the luminescence, emitted normally to the plane, with an analyzer selecting the electric field direction with the polar angle ϕ_a . Then, calculating perturbatively in $1/\Delta$ the corresponding in-plane dipole matrix element, we obtain the emitted light intensity:

$$I_{\perp}(\phi_a) \propto \left(d_{\parallel} \frac{g_{\parallel}\mu_B B_{\parallel}}{\Delta} \right)^2 \times [(\chi_+ - \chi_-)^2 + 4\chi_+\chi_- \sin^2(\phi_a + \phi_d - \phi_B)] \quad (2)$$

where $\phi_B = \arctan(B_y/B_x)$ is the polar angle of the in-

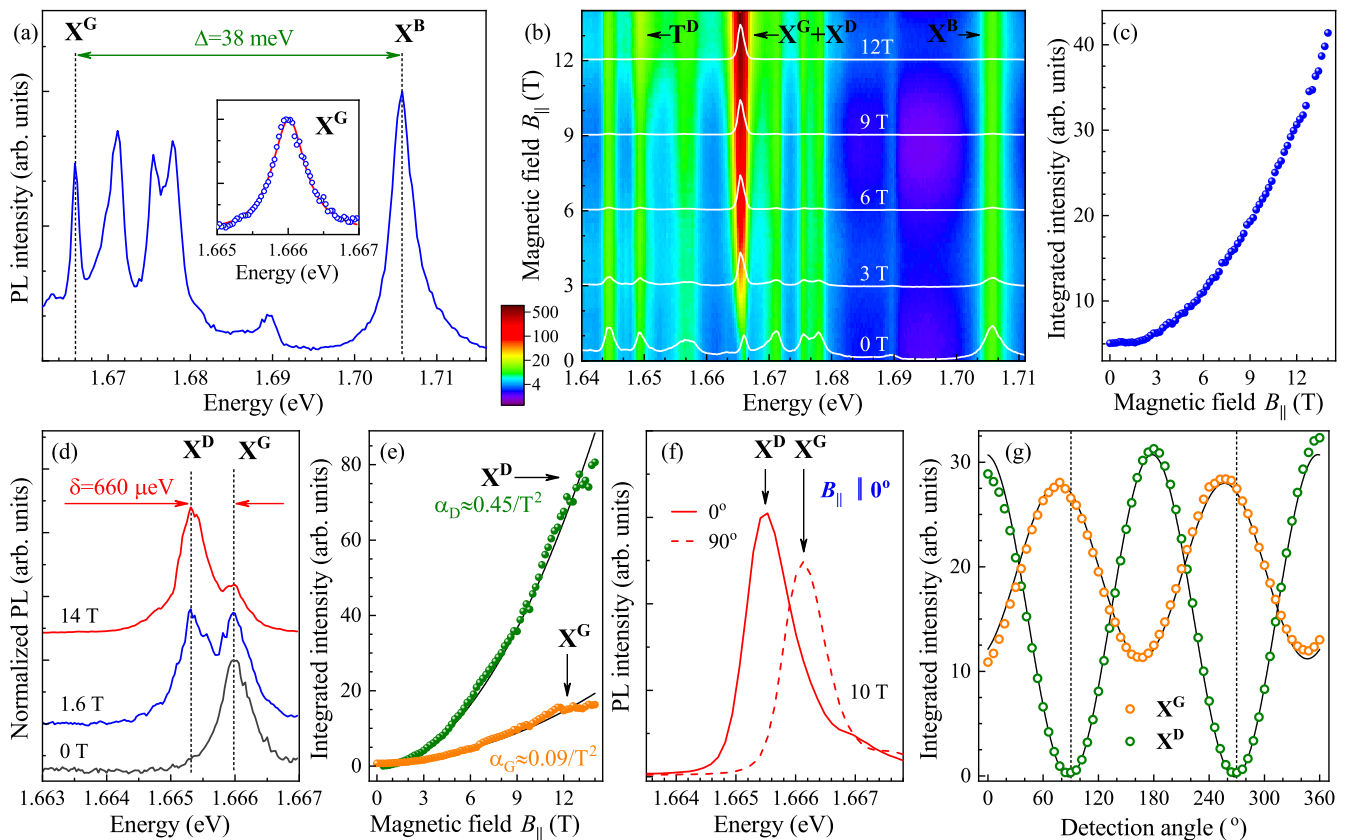


FIG. 2. (a) Low-temperature ($T=4.2$ K) PL spectrum measured on a WSe_2 monolayer encapsulated in hBN flakes, using an excitation energy 2.408 eV and a power of $50 \mu\text{W}$, and zero magnetic field. The inset shows the high-resolution PL emission of the grey exciton. (b) False-colour map of the PL response as a function of B_{\parallel} ; white curves superimposed on the map represent the PL spectra normalized to the most intense peaks recorded at selected values of B_{\parallel} . (c) Total emission as a function of B_{\parallel} (frequency integral of panel (b)). (d) High resolution PL spectra normalized to the most intense peaks at selected values of B_{\parallel} . (e) B_{\parallel} dependence of the dark and grey exciton luminescence peaks' integrated intensities. The solid black curves represent quadratic fits. (f) PL spectra at $B_{\parallel} = 10$ T recorded for two orthogonal linear polarizations oriented parallel (solid curve) and perpendicular (dashed curves) to the direction of \mathbf{B}_{\parallel} (excitation energy 1.917 eV and power $50 \mu\text{W}$). (g) Polarization dependence of the dark and grey exciton luminescence peaks' integrated intensities measured at $B_{\parallel}=10$ T.

plane magnetic field. Below we present the experimental implementation of the described tools.

Figs 2(a)-(c) illustrate the results of micro-magneto-PL measurements performed in a wide spectral range ($1.64 - 1.71$ eV), covering the whole emission spectrum of our sample, but at the expense of rather low spectral resolution (0.8 nm). In contrast, the results shown in Figs 2(d),(e) and in the inset of Fig. 2(a) refer to experiments with higher spectral resolution (0.1 nm). All spectra were measured in the configuration of the normal (to the sample plane) coincidence of the excitation and the collected beams (see Fig. 1(b) and Supplemental Material (SM) for details). The PL peaks, labelled as X^D and X^G , are ascribed, correspondingly, to dark and grey states of the neutral exciton. Only X^G is observed in the spectra measured at zero magnetic field. We expect that the X^G -emission is directed predominantly along the monolayer plane, though it is still visible in the spectra, due to a relatively high numerical aperture (NA) of the lenses

used to collect the emitted light. Both components of the X^D/X^G doublet contribute to the emission spectrum when the magnetic field is applied (see, *e.g.*, Fig. 2(d)). Note that this doublet structure is not resolved in the spectra shown in Fig. 2(b), measured with low spectral resolution. These results are in good agreement with previous reports^{2-5,10,24,35?}: (i) the grey exciton X^G -line is red-shifted by 38 meV from the emission peak X^B associated with the neutral bright exciton (see Fig. 2(a)), (ii) the energy separation between the grey (X^G) and dark (X^D) excitons is $\delta = 660 \mu\text{eV}$ (see Fig. 2(d)), and (iii) the X^D and X^G lines are much narrower (≈ 0.6 meV) than the X^B line (≈ 4 meV) what indicates the significantly longer lifetimes of dark and grey excitons as compared to the lifetime of the bright exciton (see SM for details).

Application of the in-plane magnetic field B_{\parallel} leads to a strong brightening effect, which is remarkably pronounced in our encapsulated WSe_2 monolayer, much

more than in previously probed WSe₂ monolayers on Si/SiO₂ substrates^{17,18}. This is demonstrated in Fig. 2(b) showing PL spectra measured in a wide spectral range, as a function of B_{\parallel} . With increasing B_{\parallel} , the intensity of the grey/dark exciton doublet (separate components not resolved) increases significantly, while the intensity of the bright exciton and of the lower energy features of the spectrum, stays practically at the same level. Note that the T^D line observed at about 1.65 eV in Fig. 2(b) also becomes significantly brighter at the largest magnetic fields ($B > 10$ T). Recently, this peak was ascribed to the emission of the dark negatively charged exciton⁷. In Fig. 2(c), we plot the total emission intensity (integrated over the whole PL spectrum) as a function of B_{\parallel} . At $B_{\parallel} = 14$ T, the total emission intensity is enhanced by an order of magnitude and practically the whole luminescence of the sample is due to the dark/grey excitons doublet.

The PL response of our hBN/WSe₂/hBN sample, measured with better spectral resolution, enabled us, for the first time, to resolve the magnetic brightening of the dark and grey components separately. As can be seen in Fig. 2(d), while only the grey exciton is observed when $B_{\parallel} = 0$, at fields above 1.6 T the X^D line becomes more intense. The B_{\parallel} dependence of the intensity of each component is expected to be $I = I_0 + \alpha B_{\parallel}^2$ (Refs 17,18), where the zero-field intensity I_0 vanishes for the dark component but is nonzero and depends on the NA of the excitation/detection lens for the grey component. The results of the quadratic fit are shown in Fig. 2(e). The α parameter turns out to be strongly different for the two components: $\alpha_D = 0.45 \text{ T}^{-2}$, while $\alpha_G = 0.09 \text{ T}^{-2}$. This large difference is explained by the difference in the populations of the two states: at temperature $T = 4.2$ K which corresponds to our experimental conditions, the population ratio is $e^{-\delta/k_B T} = 0.16$, in reasonable agreement with the measured ratio $\alpha_G/\alpha_D = 0.2$.

Now, one can investigate the polarization properties of magnetically brightened dark and grey excitons, see Fig. 2(f). We present in Fig. 2(g) the integrated PL intensity for each peak, as collected via the linear polarizer and measured as a function of the angle $\phi_a - \phi_B$ between the polarizer axis and the direction of the \mathbf{B}_{\parallel} field. For the dark exciton, the polarization dependence fully agrees with equation (2): indeed, at $B_{\perp} = 0$, we have $\chi_+ = -\chi_- = 1/\sqrt{2}$ and $\phi_d = 0$, resulting in the transition dipole oriented along \mathbf{B}_{\parallel} . Our polarization measurement thus reveals experimentally the nature of the dark exciton state, which is a coherent superposition of the states in the two valleys.

For the grey exciton, the measured polarization dependence corresponds to equation (2) plus a constant background. The latter is due to large NA of the lens used to collect the emitted light. Indeed, equation (2) describes emission perpendicular to the monolayer and thus is valid in the limit of small NA. Our large-NA lens picks up the light emitted by the out-of-plane component d_{\perp} of the transition dipole moment, which has no in-plane polar-

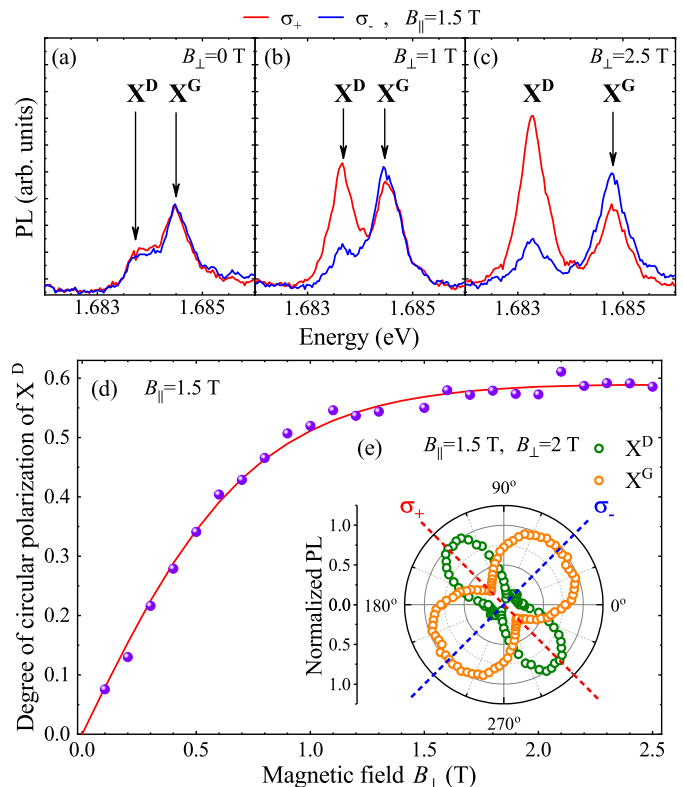


FIG. 3. (a)-(c) PL spectra of dark and grey excitons in perpendicular magnetic field applied additionally to in-plane magnetic field of 1.5 T. (d) Emergence of the circular polarization of the dark exciton upon application of additional perpendicular magnetic field. Solid red line represents a fit of function described in SM. (e) PL intensity of X^D and X^G as a function of orientation of the $\lambda/4$ waveplate in detection. Settings 45° and 135° correspond to σ_- and σ_+ polarization, respectively. The data were measured for orientations 0°-180° and cloned to 180°-360° range for the sake of presentation. Note that these results were measured on a different sample as those shown in Fig. 2.

ization. For the dark exciton at $B_{\perp} = 0$, this component is absent.

Application of a magnetic field B_{\perp} in the direction perpendicular to the monolayer plane shifts the energies in the two valleys in the opposite directions. Thus, the eigenstates in the dark-grey sector resulting from valley mixing by exchange coupling have no longer equal weights in the two valleys. As a result, both grey and dark exciton components have a finite out-of-plane optical dipole moment even at $B_{\parallel} = 0$, and are visible in the luminescence spectra due to large NA of the lens (see SM for details). Note that the intensity of the dark exciton lines is independent of the detected helicity (σ_+ or σ_-) of light.

In order to induce the σ_{\pm} selectivity for the dark excitons emission, we propose to combine the effects of parallel (B_{\parallel}) and perpendicular (B_{\perp}) magnetic fields. B_{\parallel} gives rise to linear polarizations of the grey and dark

excitons (see Fig. 2(f) and (g)), which are subsequently transformed by B_{\perp} into elliptical polarizations. The experimental evidence corroborating this scenario is presented in Fig. 3(a)-(c). Upon increasing of the B_{\perp} component of the magnetic field, both dark and grey excitons gain circular σ_{+} and σ_{-} polarizations, respectively. This allows us to determine that the g -factor of dark and grey excitons is negative as the one of the bright neutral exciton. The gradual increase in the circular degree of polarization, illustrated in Fig. 3(a)-(c), can be described in terms of the competition between the Zeeman shift $g_d\mu_B B_{\perp}$ and the initial splitting δ and taking into account a finite NA of excitation/collection lens used in experiment. The result of such competition is presented in Fig. 3(d) for the case of dark exciton emission, as an example. The blue dots (red curve) depicts the experimentally (theoretically) derived data of the circular polarization degree as a function of out-of-plane magnetic field B_{\perp} . Note that the value of the polarization degree saturates already at 60% and not at 100% as one can expect. The explanation of such phenomenon involves a finite contribution of the out-of-plane dipole components of X^D and X^G exciton states (see SM for details). To prove the dominant contribution of the circular polarization (σ_{\pm}) for the dark and grey exciton emissions, they were measured as a function of orientation of the $\lambda/4$ waveplate in detection, see Fig. 3(f).

In this work, we investigated the PL response of a

hBN-encapsulated WSe_2 monolayer subject to a magnetic field, whose direction lies in the monolayer plane, or perpendicular to it. Thanks to the encapsulation, the in-plane field leads to a very pronounced brightening effect on the dark lowest-energy excitons in WSe_2 , and most of the sample's luminescence comes from these dark excitons. Moreover, in our encapsulated sample one can resolve the fine structure of the magnetically brightened dark excitons, split by the exchange interaction which produces two coherent valley superpositions as eigenstates. We were able to probe the coefficients of the superpositions by a polarization-resolved PL measurement. These coefficients can be changed by applying a perpendicular and/or parallel magnetic field. These findings open a perspective for controlled manipulation of the valley degree of freedom of long-lived dark excitons in monolayer S-TMDs.

The work has been supported by the ATOMOPTO project (TEAM programme of the Foundation for Polish Science, co-financed by the EU within the ERDFund), the EU Graphene Flagship project (no. 785219), the National Science Centre, Poland (grant no. UMO-2018/31/B/ST3/02111), the Nanofab facility of the Institut Néel, CNRS/UGA and the LNCMI-CNRS, a member of the European Magnetic Field Laboratory (EMFL). K.W. and T.T. acknowledge support from the Elemental Strategy Initiative conducted by the MEXT, Japan and the CREST (JPMJCR15F3), JST.

-
- ¹ K. F. Mak, C. Lee, J. Hone, J. Shan, and T. F. Heinz, *Phys. Rev. Lett.* **105**, 136805 (2010).
- ² Q. H. Wang, K.-Z. Kouros, A. Kis, J. N. Coleman, and M. S. Strano, *Nature Nanotechnology* **7**, 699 (2012).
- ³ G. Eda and S. A. Maier, *ACS Nano* **7**, 5660 (2013).
- ⁴ F. Xia, H. Wang, D. Xiao, M. Dubey, and A. Ramasubramaniam, *Nature Photonics* **8**, 899 (2014).
- ⁵ X. Xu, W. Yao, D. Xiao, and T. F. Heinz, *Nature Physics* **10**, 343 (2014).
- ¹⁸ M. Koperski, M. R. Molas, A. Arora, K. Nogajewski, A. O. Slobodeniuk, C. Faugeras, and P. M., *Nanophotonics* **6**, 1289 (2017).
- ⁷ G. Wang, A. Chernikov, M. M. Glazov, T. F. Heinz, X. Marie, T. Amand, and B. Urbaszek, *Rev. Mod. Phys.* **90**, 021001 (2018).
- ⁸ A. Chernikov, T. C. Berkelbach, H. M. Hill, A. Rigosi, Y. Li, O. B. Aslan, D. R. Reichman, M. S. Hybertsen, and T. F. Heinz, *Phys. Rev. Lett.* **113**, 076802 (2014).
- ⁹ Z. Ye, T. Cao, K. O'Brien, H. Zhu, X. Yin, Y. Wang, S. G. Louie, and X. Zhang, *Nature* **513**, 214 (2014).
- ¹⁰ M. M. Ugeda, A. J. Bradley, S.-F. Shi, F. H. da Jornada, Y. Zhang, D. Y. Qiu, W. Ruan, S.-K. Mo, Z. Hussain, Z.-X. Shen, F. Wang, S. G. Louie, and M. F. Crommie, *Nature Materials* **13**, 1091 (2014).
- ¹¹ K. He, N. Kumar, L. Zhao, Z. Wang, K. F. Mak, H. Zhao, and J. Shan, *Phys. Rev. Lett.* **113**, 026803 (2014).
- ¹² W. Yao, D. Xiao, and Q. Niu, *Phys. Rev. B* **77**, 235406 (2008).
- ¹³ D. Xiao, G.-B. Liu, W. Feng, X. Xu, and W. Yao, *Phys. Rev. Lett.* **108**, 196802 (2012).
- ¹⁴ K. Kośmider, J. W. González, and J. Fernández-Rossier, *Phys. Rev. B* **88**, 245436 (2013).
- ¹⁵ A. Kormányos, G. Burkard, M. Gmitra, J. Fabian, V. Zólyomi, N. D. Drummond, and V. Fal'ko, *2D Materials* **2**, 022001 (2015).
- ¹⁶ J. P. Echeverry, B. Urbaszek, T. Amand, X. Marie, and I. C. Gerber, *Phys. Rev. B* **93**, 121107(R) (2016).
- ¹⁷ M. R. Molas, C. Faugeras, A. O. Slobodeniuk, K. Nogajewski, M. Bartos, D. M. Basko, and M. Potemski, *2D Materials* **4**, 021003 (2017).
- ¹⁸ X.-X. Zhang, T. Cao, Z. Lu, Y.-C. Lin, F. Zhang, Y. Wang, Z. Li, J. C. Hone, J. A. Robinson, D. Smirnov, S. G. Louie, and T. F. Heinz, *Nature Nanotechnology* **12**, 883 (2017).
- ¹⁹ A. Arora, M. Koperski, K. Nogajewski, J. Marcus, C. Faugeras, and M. Potemski, *Nanoscale* **7**, 10421 (2015).
- ⁸ X.-X. Zhang, Y. You, S. Zhao, and T. F. Heinz, *Phys. Rev. Lett.* **115**, 257403 (2015).
- ²¹ G. Wang, C. Robert, A. Suslu, B. Chen, S. Yang, S. Alamdari, I. C. Gerber, T. Amand, X. Marie, S. Tongay, and B. Urbaszek, *Nature Comm.* **6**, 10110 (2015).
- ²² M. M. Glazov, T. Amand, X. Marie, D. Lagarde, L. Bouet, and B. Urbaszek, *Phys. Rev. B* **89**, 201302(R) (2014).
- ²³ A. O. Slobodeniuk and D. M. Basko, *2D Materials* **3**, 035009 (2016).
- ²⁴ G. Wang, C. Robert, M. M. Glazov, F. Cadiz, E. Courtade, T. Amand, D. Lagarde, T. Taniguchi, K. Watanabe, B. Urbaszek, and X. Marie, *Phys. Rev. Lett.* **119**, 047401 (2017).

- ²⁵ H. Dery and Y. Song, *Phys. Rev. B* **92**, 125431 (2015).
- ²⁶ H. Zeng, J. Dai, W. Yao, D. Xiao, and X. Cui, *Nature Nanotechnology* **7**, 490 (2012).
- ²⁷ K. F. Mak, K. He, J. Shan, and T. F. Heinz, *Nature Nanotechnology* **7**, 494 (2012).
- ²⁸ A. M. Jones, H. Yu, N. J. Ghimire, S. Wu, G. Aivazian, J. S. Ross, B. Zhao, J. Yan, D. G. Mandrus, D. Xiao, W. Yao, and X. Xu, *Nature Nanotechnology* **8**, 634 (2013).
- ¹² G. Aivazian, Z. Gong, A. M. Jones, R.-L. Chu, J. Yan, D. G. Mandrus, C. Zhang, D. Cobden, W. Yao, and X. Xu, *Nature Physics* **11**, 148 (2015).
- ³⁰ G. Wang, X. Marie, B. L. Liu, T. Amand, C. Robert, F. Cadiz, P. Renucci, and B. Urbaszek, *Phys. Rev. Lett.* **117**, 187401 (2016).
- ³¹ T. Smoleński, M. Goryca, M. Koperski, C. Faugeras, T. Kazimierczuk, A. Bogucki, K. Nogajewski, P. Kossacki, and M. Potemski, *Phys. Rev. X* **6**, 021024 (2016).
- ³² K. Hao, G. Moody, F. Wu, C. K. Dass, L. Xu, C.-H. Chen, L. Sun, M.-Y. Li, L.-J. Li, A. H. MacDonald, and X. Li, *Nature Physics* **12**, 677 (2016).
- ¹⁰ C. Robert, T. Amand, F. Cadiz, D. Lagarde, E. Courtade, M. Manca, T. Taniguchi, K. Watanabe, B. Urbaszek, and X. Marie, *Phys. Rev. B* **96**, 155423 (2017).
- ³⁴ Z. Wang, J. Shan, and K. F. Mak, *Nature Nanotechnology* **12**, 144 (2016).
- ³⁵ F. Cadiz, E. Courtade, C. Robert, G. Wang, Y. Shen, H. Cai, T. Taniguchi, K. Watanabe, H. Carrere, D. Lagarde, M. Manca, T. Amand, P. Renucci, S. Tongay, X. Marie, and B. Urbaszek, *Phys. Rev. X* **7**, 021026 (2017).
- ³⁶ O. A. Ajayi, J. V. Ardelean, G. D. Shepard, J. Wang, A. Antony, T. Taniguchi, K. Watanabe, T. F. Heinz, S. Strauf, X.-Y. Zhu, and J. C. Hone, *2D Materials* **4**, 031011 (2017).
- ³⁷ M. Manca, C. R. M.M. Glazov, T. T. F. Cadiz, E. C. K. Watanabe, P. R. T. Amand, G. W. X. Marie, and B. Urbaszek, *Nat. Commun.* **8**, 14927 (2017).
- ³⁸ D. Vaclavkova, J. Wyzula, K. Nogajewski, M. Bartos, A. O. Slobodeniuk, C. Faugeras, M. Potemski, and M. R. Molas, *Nanotechnology* **29**, 325705 (2018).
- ³⁹ A. O. Slobodeniuk and D. M. Basko, *2D Materials* **6**, 029501 (2019).

Supplemental Material: Probing and manipulating valley coherence of dark excitons in monolayer WSe₂

M. R. Molas,^{1,2} A. O. Slobodeniuk,¹ T. Kazimierczuk,² K. Nogajewski,^{1,2} M. Bartos,¹ P. Kapuściński,^{1,3}
K. Oreszczuk,² K. Watanabe,⁴ T. Taniguchi,⁴ C. Faugeras,¹ D. M. Basko,⁵ and M. Potemski,^{1,2}

¹ *Laboratoire National des Champs Magnétiques Intenses, CNRS-UGA-UPS-INSA-EMFL, 25, avenue des Martyrs, 38042 Grenoble, France*

² *Faculty of Physics, University of Warsaw, ul. Pasteura 5, 02-093 Warszawa, Poland*

³ *Department of Experimental Physics, Faculty of Fundamental Problems of Technology, Wrocław University of Science and Technology, 27 Wybrzeże Wyspiańskiego, 50-370 Wrocław, Poland*

⁴ *National Institute for Materials Science, 1-1 Namiki, Tsukuba 305-0044, Japan*

⁵ *Laboratoire de Physique et Modélisation des Milieux Condensés, Université Grenoble Alpes and CNRS, 25 avenue des Martyrs, 38042 Grenoble, France*

This supplemental material provides: [S1](#) description of preparation of the studied samples and used experimental setups, [S2](#) low-temperature photoluminescence spectrum measured on the studied sample, [S3](#) the influence of in-plane magnetic field on lifetimes of dark and grey excitons, [S4](#) the effect of perpendicular magnetic field on grey and dark excitons emissions, and [S5](#) polarization properties of dark excitons emission.

S1. Samples and experimental setups

The active part of our sample consists of a monolayer of WSe₂, which has been encapsulated in hexagonal boron nitride (hBN) and deposited on a bare Si substrate. It was fabricated by two-stage polydimethylsiloxane (PDMS)-based⁷ mechanical exfoliation of WSe₂ and hBN bulk crystals. Micro-magneto-photoluminescence (PL) measurements (spatial resolution $\sim 5 \mu\text{m}$) were carried out at liquid helium temperature using two different experimental setups. In each setup, the sample was placed on top of a $x - y - z$ piezo-stage kept at $T=4.2$ K and was excited using laser diodes with either 515 nm wavelength (2.408 eV photon energy) or 647 nm wavelength (1.917 eV photon energy). The emitted light was dispersed with a 0.5 m long monochromator and detected with a charge coupled device (CCD) camera. The data presented in Figs 2(a)-(e) and [S3](#) refer to measurements performed with the fiber-optic based setup and were carried out in magnetic fields up to 14 T. Unpolarized emission was measured in Voigt configuration (see Fig. 2(a)-(e)), whereas the σ_- and σ_+ -polarized components of the emitted light were resolved in experiments (see Fig. [S3](#)) performed in the Faraday configuration (polarizers placed in a close vicinity of the sample, in between the sample and optical fibers). The data presented in Figs 2(f)-(g) refer to experiments carried out using a split-coil (10 T) superconducting magnet with a free-beam-optics arrangement. Fig. 3 illustrates results obtained with the aid of a system of two split-coil superconducting magnets with a free-beam-optics arrangement allowing to apply independently in-plane and out-of-plane magnetic fields. The linear and circular polarizations of the emissions were analyzed using a set of polarizers and waveplates ($\lambda/2$ and $\lambda/4$) placed directly in front of the spectrometers. The data presented in Figs 2, 3, [S1](#) and [S3](#) refer to spectra measured with different spectral resolutions: 0.8 nm — Figs 2(a)-(c), [S1](#) and [S3](#); 0.2 nm — Fig. 2(f)-(g); 0.1 nm — the inset of Fig. 2(a), Fig. 2(d)-(e) and Fig. 3.

S2. Low-temperature PL spectrum of the WSe₂ monolayer

Fig. [S1](#) demonstrates the photoluminescence spectrum measured on a WSe₂ monolayer encapsulated in hBN flakes. The PL spectrum displays several emission lines with a similar characteristic pattern already reported in a number of previous works on WSe₂ monolayers embedded in between hBN flakes²⁻⁷. In accordance with these reports, the assignment of the observed emission lines is as follows: X^B — a bright neutral exciton formed in the vicinity of the A exciton; XX — a neutral biexciton; T^S and T^T — singlet (intravalley) and triplet (intervalley) negatively charged excitons, respectively; X^G — a grey exciton; XX⁻ — a negatively charged biexciton; T^D — a negatively charged dark exciton; L₁ — a so-called localized exciton. The attribution of the P line is not clear, as in the most reported PL spectra this peak was absent³⁻⁷, but was observed in the neutral regime (between n and p -type doping) in Ref. [2](#). As the energy separation between X^B and P lines of about 31 meV is close to the longitudinal optical (LO) phonon energy ($E_{\text{LO}}=32$ meV⁸), we ascribed tentatively this peak to the LO phonon replica of the bright neutral exciton.

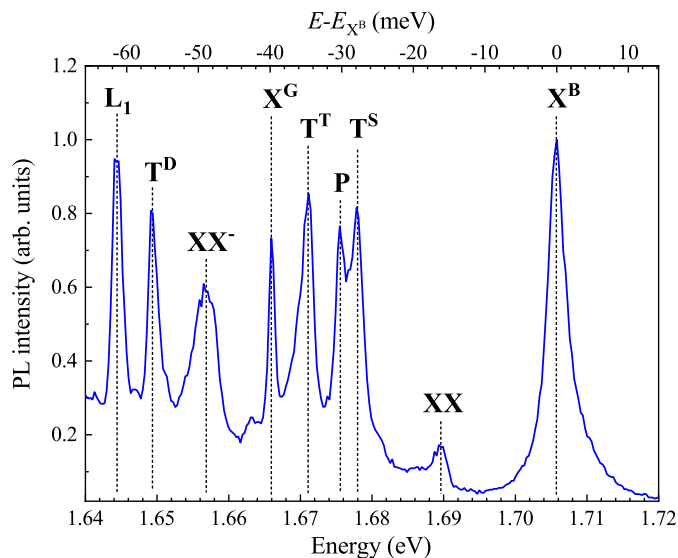


FIG. S1. Low-temperature ($T=4.2$ K) PL spectrum measured on a WSe_2 monolayer encapsulated in hBN flakes, using an excitation energy 2.408 eV and a power of $50 \mu\text{W}$, and zero magnetic field.

S3. The influence of in-plane magnetic field on lifetimes of grey and dark excitons

To get more information on the grey and dark excitons, we measured their lifetimes by time-resolved photoluminescence spectroscopy, when an in-plane magnetic field is applied. Fig. S2(a) shows the X^G and X^D emissions kinetics following a pulsed laser excitation, while Fig. S2(b) summarizes their obtained decay times for a few values of magnetic fields. We found that the grey and dark excitons lifetimes are on the order of hundreds ps and are significantly longer as compared to the reported ~ 2 ps lifetime of the bright neutral exciton in WSe_2 monolayer^{9,10}. As can be appreciated in Fig. S3(b), we do not observe an effect of an in-plane magnetic field on the X^G and X^D lifetimes. Consequently, the extrapolated values of the grey and dark excitons at zero magnetic field are of about 220 ps and 250 ps, respectively. We note also that the obtained X^G lifetime is almost two time larger than the reported previously in Ref. 10.

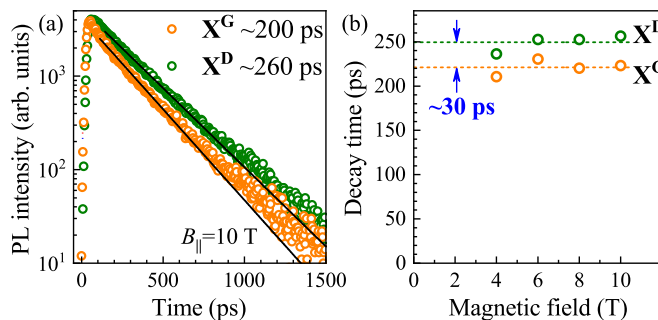


FIG. S2. (a) Low-temperature ($T=4.2$ K) time resolved PL measured on a WSe_2 monolayer encapsulated in hBN flakes under in-plane magnetic field $B_{\parallel}=10$ T, (b) The obtained decay times of the X^G and X^D lines for a few magnetic fields.

S4. The effect of perpendicular magnetic field on grey and dark excitons emissions

The magneto-luminescence spectra for two opposite circular polarizations, measured in the Faraday configuration are shown in Fig. S3 a. The bright exciton emission splits into two circularly polarized components centered at energies $E_{b,\pm} = E_B \pm g_b \mu_B B_{\perp}/2$, due to the valley Zeeman effect, as can be appreciated at the top of Fig. S3a,b. We obtain $g_b = -4.2$, in agreement with previously reported values¹⁰⁻¹⁵.

The magnetic field evolution of the dark and grey exciton peaks is different. First, the intensity of dark(grey)

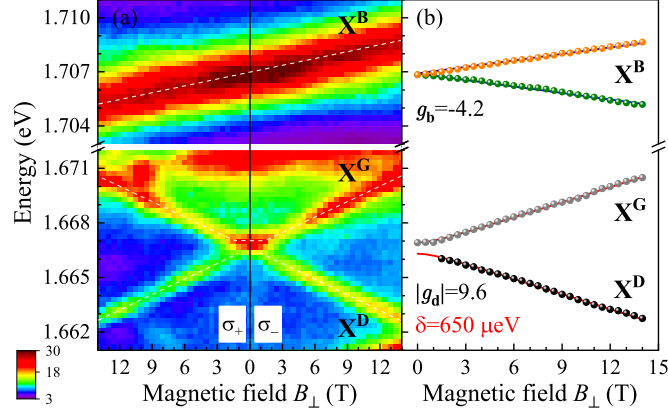


FIG. S3. (a) False-colour map of the helicity-resolved (σ_{\pm}) PL spectra as a function of B_{\perp} (excitation energy 2.408 eV and power 50 μW). The dashed white lines are guides to the eye. (b) Magnetic field dependence of the dark and bright exciton energies. The green and orange points correspond to the σ_+ - and σ_- -polarized components of the bright exciton resonance, respectively. The grey and black points denote correspondingly the averaged energies of the grey and dark excitons for both circular polarizations. The solid blue and red curves represent fits with $E_{b,\pm} = E_B \pm g_b \mu_B B_{\perp} / 2$ and equation (3), respectively.

exciton line is the same in both circular polarizations. Secondly, the peak energies are separated by the exchange gap δ :

$$E_{G,D} = E_d \pm \frac{1}{2} \sqrt{\delta^2 + (g_d \mu_B B_{\perp})^2}. \quad (3)$$

From the fit we extract $\delta = 650 \mu\text{eV}$ and $|g_d| = 9.6$, in agreement with Ref. 10 ($\delta = 600 \mu\text{eV}$ and $|g_d| = 9.4$) and our measurements in the in-plane field, described above ($\delta = 660 \mu\text{eV}$). In the single particle picture, the Zeeman shift in a perpendicular magnetic field has two contributions: the spin and the valley-orbital^{11,12,15–18}. The latter is the same for bright and dark excitons from the same valley. Hence, from the difference in the g factors of dark and bright excitons we can extract the spin g factor in the conduction band, which amounts to 2.7. Note that due to the results performed in combination of the in-plane and out-of-plane magnetic fields, we were able to determine that the grey-dark g -factor is negative similarly as for the bright neutral exciton and equals $g_d = -9.4$.

S5. Polarization properties of dark excitons emission

We consider the lowest energy (dark) exciton states of S-TMD monolayer in the presence of non-zero out-of-plane B_{\perp} and in-plane \mathbf{B}_{\parallel} magnetic fields. B_{\perp} couples $|\mathbf{K}_{+}, d\rangle$ and $|\mathbf{K}_{-}, d\rangle$ dark states of opposite valleys. \mathbf{B}_{\parallel} mixes bright $|\mathbf{K}_{\pm}, b\rangle$ and dark $|\mathbf{K}_{\pm}, d\rangle$ states within the same valley. Taking into account both effects and considering the bright-dark exciton coupling perturbatively in the parameter $g_{\parallel} \mathcal{B}_{\parallel} / \Delta \equiv g_{\parallel} \mu_B |\mathbf{B}_{\parallel}| / 2\Delta \ll 1$, one derives the lowest energy exciton states

$$|D_h\rangle = \mathcal{N} \left[-\frac{g_{\parallel} \mathcal{B}_{\parallel}}{\Delta} e^{-i\phi_B} \sin\left(\frac{\vartheta}{2} + \frac{\pi}{4}\right), -\frac{g_{\parallel} \mathcal{B}_{\parallel}}{\Delta} e^{i\phi_B} \cos\left(\frac{\vartheta}{2} + \frac{\pi}{4}\right), \sin\left(\frac{\vartheta}{2} + \frac{\pi}{4}\right), \cos\left(\frac{\vartheta}{2} + \frac{\pi}{4}\right) \right], \quad (4)$$

$$|D_l\rangle = \mathcal{N} \left[-\frac{g_{\parallel} \mathcal{B}_{\parallel}}{\Delta} e^{-i\phi_B} \cos\left(\frac{\vartheta}{2} + \frac{\pi}{4}\right), \frac{g_{\parallel} \mathcal{B}_{\parallel}}{\Delta} e^{i\phi_B} \sin\left(\frac{\vartheta}{2} + \frac{\pi}{4}\right), \cos\left(\frac{\vartheta}{2} + \frac{\pi}{4}\right), -\sin\left(\frac{\vartheta}{2} + \frac{\pi}{4}\right) \right], \quad (5)$$

written in the basis $\{|\mathbf{K}_{+}, b\rangle, |\mathbf{K}_{-}, b\rangle, |\mathbf{K}_{+}, d\rangle, |\mathbf{K}_{-}, d\rangle\}$. Here $\vartheta = \arcsin \left[g_d \mu_B B_{\perp} / \sqrt{\delta^2 + (g_d \mu_B B_{\perp})^2} \right] \in [-\pi/2, \pi/2]$ and $\mathcal{N} = 1 / \sqrt{1 + (g_{\parallel} \mathcal{B}_{\parallel} / \Delta)^2}$. The indices h and l represent the higher and lower energy branches of these new exciton states, with corresponding energies up to quadratic in $g_{\parallel} \mathcal{B}_{\parallel} / \Delta$ terms

$$\begin{pmatrix} E_h \\ E_l \end{pmatrix} = \frac{\delta}{2} \pm \frac{1}{2} \sqrt{\delta^2 + (g_d \mu_B B_{\perp})^2} - \frac{(g_{\parallel} \mu_B \mathbf{B}_{\parallel})^2}{4\Delta}. \quad (6)$$

Note that $|D_h\rangle$ and $|D_l\rangle$ states turn into gray $|G\rangle$ and dark $|D\rangle$ ones respectively in the limit of the zero magnetic field. Therefore, one can call $|D_h\rangle$ and $|D_l\rangle$ also dark exciton states for brevity.

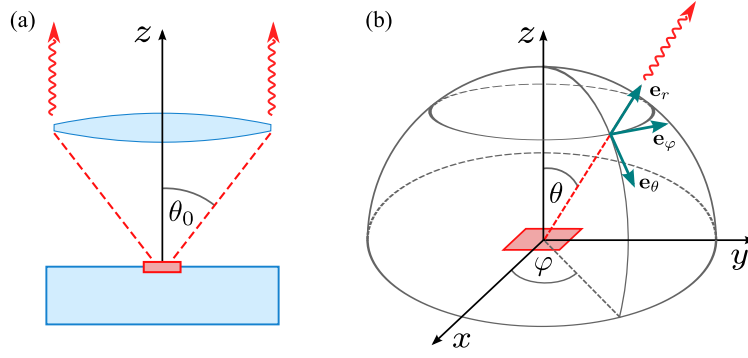


FIG. S4. (a) The side view of the main part of the setup. Red dashed lines represent the solid angle (with colatitude θ_0), all the photons inside which are absorbed by the lens. The wavy arrows represent the photons outgoing from the lens. The red rectangular in the focus of the lens depicts S-TMD sample placed on Si/SiO₂ substrate (blue rectangular). (b) The schematic view of the trace of photons (dashed red line), emitted from the sample (red parallelogram) in the (θ, φ) direction. Three blue-green arrows represent the spherical basis vectors.

The new dark excitons are optically active and their radiation patterns can be determined from the corresponding transition dipole matrix elements

$$\langle 0|\mathbf{d}|D_h\rangle = i\mathcal{N}d_{\parallel}\frac{g_{\parallel}\mathcal{B}_{\parallel}}{\Delta}\left\{e^{-i\phi_B}\sin\left(\frac{\vartheta}{2}+\frac{\pi}{4}\right)[\mathbf{e}_x+i\mathbf{e}_y]+e^{i\phi_B}\cos\left(\frac{\vartheta}{2}+\frac{\pi}{4}\right)[- \mathbf{e}_x+i\mathbf{e}_y]\right\}+i\mathcal{N}\sqrt{2}d_{\perp}\cos\left(\frac{\vartheta}{2}\right)\mathbf{e}_z, \quad (7)$$

$$\langle 0|\mathbf{d}|D_l\rangle = i\mathcal{N}d_{\parallel}\frac{g_{\parallel}\mathcal{B}_{\parallel}}{\Delta}\left\{e^{-i\phi_B}\cos\left(\frac{\vartheta}{2}+\frac{\pi}{4}\right)[\mathbf{e}_x+i\mathbf{e}_y]-e^{i\phi_B}\sin\left(\frac{\vartheta}{2}+\frac{\pi}{4}\right)[- \mathbf{e}_x+i\mathbf{e}_y]\right\}-i\mathcal{N}\sqrt{2}d_{\perp}\sin\left(\frac{\vartheta}{2}\right)\mathbf{e}_z. \quad (8)$$

Both dipole vectors have the structure $\mathbf{d}_{\alpha}\equiv\langle 0|\mathbf{d}|D_{\alpha}\rangle=a_{\alpha}[\mathbf{e}_x+i\mathbf{e}_y]+b_{\alpha}[-\mathbf{e}_x+i\mathbf{e}_y]+c_{\alpha}\mathbf{e}_z$, $\alpha=h,l$ and can be considered simultaneously.

The polarization degree of dark exciton emission is defined as

$$P_{\alpha}=\frac{I_{\alpha}(\sigma_{+})-I_{\alpha}(\sigma_{-})}{I_{\alpha}(\sigma_{+})+I_{\alpha}(\sigma_{-})}. \quad (9)$$

Here $I_{\alpha}(\sigma_{\pm})$ is the total intensity of the σ_{\pm} polarized light passing through the lens (see Fig. S4(a)). $I_{\alpha}(\sigma_{\pm})$ can be estimated by calculating the number of σ_{\pm} polarized photons propagating inside the solid angle, defined by the colatitude θ_0 . We assume that the sample is placed in the focus of the lens, its size is much smaller than the size of the lens, and that the circular polarization of a photon is not affected as it passes through the lens.

The amount of σ_{\pm} polarized photons, which are emitted from the sample, depends on the direction of their propagation. This direction is defined by spherical angles (θ, φ) or radial unit vector \mathbf{e}_r (see Fig. S4(b)). The corresponding total intensities of light with fixed polarization can be evaluated as the integral

$$I_{\alpha}(\sigma_{\pm})\propto\int_0^{2\pi}d\varphi\int_0^{\theta_0}\sin\theta d\theta|\mathbf{d}_{\alpha}\cdot\mathbf{e}_{\pm}(\theta,\varphi)|^2. \quad (10)$$

Here $\mathbf{e}_{\pm}(\theta, \varphi)$ are the polarization vectors of the σ_{\pm} polarized photons propagating in the direction defined by the angles (θ, φ) . In order to write \mathbf{e}_{\pm} explicitly, we introduce the local orthogonal unit vectors in the directions of increasing r , θ and φ , respectively (see Fig. S4 b)

$$\mathbf{e}_r=\sin\theta\cos\varphi\mathbf{e}_x+\sin\theta\sin\varphi\mathbf{e}_y+\cos\theta\mathbf{e}_z, \quad (11)$$

$$\mathbf{e}_{\theta}=\cos\theta\cos\varphi\mathbf{e}_x+\cos\theta\sin\varphi\mathbf{e}_y-\sin\theta\mathbf{e}_z, \quad (12)$$

$$\mathbf{e}_{\varphi}=-\sin\varphi\mathbf{e}_x+\cos\varphi\mathbf{e}_y. \quad (13)$$

The spherical basis $\{\mathbf{e}_{\theta}, \mathbf{e}_{\varphi}, \mathbf{e}_r\}$ has the same relative orientation as $\{\mathbf{e}_x, \mathbf{e}_y, \mathbf{e}_z\}$. Hence, it is natural to define $\mathbf{e}_{\pm}(\theta, \varphi)\equiv(\pm\mathbf{e}_{\theta}+i\mathbf{e}_{\varphi})/\sqrt{2}$. Taking the corresponding scalar products

$$\mathbf{d}_{\alpha}\cdot\mathbf{e}_{\pm}(\theta,\varphi)=-\frac{a_{\alpha}}{\sqrt{2}}(1\mp\cos\theta)e^{i\varphi}-\frac{b_{\alpha}}{\sqrt{2}}(1\pm\cos\theta)e^{-i\varphi}\mp\frac{c_{\alpha}}{\sqrt{2}}\sin\theta, \quad (14)$$

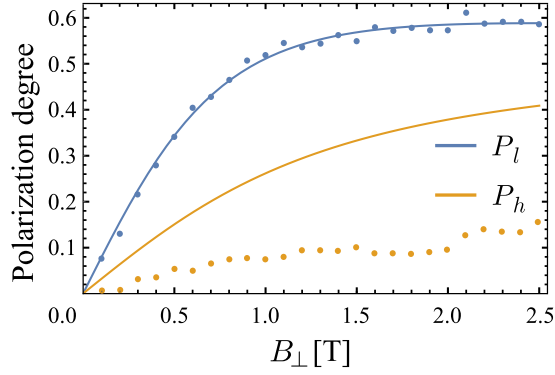


FIG. S5. Absolute values of the polarization degrees of lower (P_l) and higher-energy (P_h) dark excitons as a function of the out-of-plane magnetic field B_\perp . Blue and yellow dots depict the corresponding experimental data. Blue line represents the best fit for lower-energy dark excitons, with parameters $\theta_0 = 1.139 \approx 65^\circ$ and $d_\perp/d_\parallel = 0.0035$. Yellow line corresponds to P_h curve with the same parameters.

and then using (10) we obtain

$$P_\alpha = \frac{6(|b_\alpha|^2 - |a_\alpha|^2) \cos^2\left(\frac{\theta_0}{2}\right)}{(|b_\alpha|^2 + |a_\alpha|^2)(4 + \cos\theta_0 + \cos^2\theta_0) + 2|c_\alpha|^2 \sin^2\left(\frac{\theta_0}{2}\right)(2 + \cos\theta_0)}. \quad (15)$$

Finally, the expressions for polarization degrees of higher-energy and lower-energy states read

$$P_h = \frac{-6 \cos^2\left(\frac{\theta_0}{2}\right) \sin\vartheta}{4 + \cos\theta_0 + \cos^2\theta_0 + \left(\frac{4\Delta}{g_\parallel \mu_B B_\parallel} \frac{d_\perp}{d_\parallel}\right)^2 \sin^2\left(\frac{\theta_0}{2}\right)(2 + \cos\theta_0) \cos^2\left(\frac{\vartheta}{2}\right)}, \quad (16)$$

$$P_l = \frac{6 \cos^2\left(\frac{\theta_0}{2}\right) \sin\vartheta}{4 + \cos\theta_0 + \cos^2\theta_0 + \left(\frac{4\Delta}{g_\parallel \mu_B B_\parallel} \frac{d_\perp}{d_\parallel}\right)^2 \sin^2\left(\frac{\theta_0}{2}\right)(2 + \cos\theta_0) \sin^2\left(\frac{\vartheta}{2}\right)}. \quad (17)$$

We fit the experimental data for lower-energy dark excitons polarization degree using the following parameters: $\Delta = 38$ meV, $\mu_B = 0.05788$ meV/T, $B_\parallel = |\mathbf{B}_\parallel| = 1.5$ T, $|g_d| = 9.6$, $g_\parallel = 2$, $\delta = 0.65$ meV. The best fit corresponds to $\theta_0 = 1.139 \approx 65^\circ$ and $d_\perp/d_\parallel = 0.0035$, and is represented by a blue curve in Fig. S5. Using the same parameters we plot the curve for polarization degree for higher-energy dark excitons, see an orange curve in Fig. S5. For the considered range of parameters, the second curve approximates badly the corresponding experimental points. Probably, in the latter case there are additional unaccounted mechanisms, which reduce strongly the polarization degree of higher-energy exciton states.

-
- ¹ A. Castellanos-Gomez, M. Buscema, R. Molenaar, V. Singh, L. Janssen, H. S. J. van der Zant, and G. A. Steele, 2D Materials **1**, 011002 (2014).
 - ² E. Courtade, M. Semina, M. Manca, M. M. Glazov, C. Robert, F. Cadiz, G. Wang, T. Taniguchi, K. Watanabe, M. Pierre, W. Escoer, E. L. Ivchenko, P. Renucci, X. Marie, T. Amand, and B. Urbaszek, Phys. Rev. B **96**, 085302 (2017).
 - ³ Z. Li, T. Wang, Z. Lu, C. Jin, Y. Chen, Y. Meng, Z. Lian, T. Taniguchi, K. Watanabe, S. Zhang, D. Smirnov, and S.-F. Shi, Nature Communications **9**, 3719 (2018).
 - ⁴ S.-Y. Chen, T. Goldstein, T. Taniguchi, K. Watanabe, and J. Yan, Nature Communications **9**, 3717 (2018).
 - ⁵ M. Barbone, A. R. P. Montblanch, D. M. Kara, C. Palacios-Berraquero, A. R. Cadore, D. De Fazio, B. Pingault, E. Mostaani, H. Li, B. Chen, K. Watanabe, T. Taniguchi, S. Tongay, G. Wang, A. C. Ferrari, and M. Atature, Nature Communications **9**, 3721 (2018).
 - ⁶ M. Paur, A. J. Molina-Mendoza, R. Bratschitsch, K. Watanabe, T. Taniguchi, and T. Mueller, Nature Communications **10**, 1709 (2019).
 - ⁷ E. Liu, J. van Baren, Z. Lu, M. M. Altairy, T. Taniguchi, K. Watanabe, D. Smirnov, and C. H. Lui, arXiv e-prints (2019), arXiv:1901.11043 [cond-mat.mtrl-sci].
 - ⁸ X.-X. Zhang, Y. You, S. Y. F. Zhao, and T. F. Heinz, Phys. Rev. Lett. **115**, 257403 (2015).
 - ⁹ C. Robert, D. Lagarde, F. Cadiz, G. Wang, B. Lassagne, T. Amand, A. Balocchi, P. Renucci, S. Tongay, B. Urbaszek, and X. Marie, Phys. Rev. B **93**, 205423 (2016).

- ¹⁰ C. Robert, T. Amand, F. Cadiz, D. Lagarde, E. Courtade, M. Manca, T. Taniguchi, K. Watanabe, B. Urbaszek, and X. Marie, *Phys. Rev. B* **96**, 155423 (2017).
- ¹¹ A. Srivastava, M. Sidler, A. V. Allain, D. S. Lembke, A. Kis, and A. Imamoglu, *Nature Physics* **11**, 141 (2015).
- ¹² G. Aivazian, Z. Gong, A. M. Jones, R.-L. Chu, J. Yan, D. G. Mandrus, C. Zhang, D. Cobden, W. Yao, and X. Xu, *Nature Physics* **11**, 148 (2015).
- ¹³ G. Wang, L. Bouet, M. M. Glazov, T. Amand, E. L. Ivchenko, E. Palleau, X. Marie, and B. Urbaszek, *2D Materials* **2**, 034002 (2015).
- ¹⁴ A. A. Mitioglu, P. Plochocka, A. Granados del Aguila, P. C. M. Christianen, G. Deligeorgis, S. Anghel, L. Kulyuk, and D. K. Maude, *Nano Letters* **15**, 4387 (2015).
- ¹⁵ M. Koperski, M. R. Molas, A. Arora, K. Nogajewski, M. Bartos, J. Wyzula, D. Vaclavkova, P. Kossacki, and M. Potemski, *2D Materials* **6**, 015001 (2019).
- ¹⁶ Y. Li, J. Ludwig, T. Low, A. Chernikov, X. Cui, G. Arefe, Y. D. Kim, A. M. van der Zande, A. Rigosi, H. M. Hill, S. H. Kim, J. Hone, Z. Li, D. Smirnov, and T. F. Heinz, *Phys. Rev. Lett.* **113**, 266804 (2014).
- ¹⁷ D. MacNeill, C. Heikes, K. F. Mak, Z. Anderson, A. Kormanyos, V. Zolyomi, J. Park, and D. C. Ralph, *Phys. Rev. Lett.* **114**, 037401 (2015).
- ¹⁸ M. Koperski, M. R. Molas, A. Arora, K. Nogajewski, A. O. Slobodeniuk, C. Faugeras, and P. M., *Nanophotonics* **6**, 1289 (2017).